buildings

MDPI

Article

Characterization of Three-Dimensional Strong Force Chain Properties of Mineral Aggregate Mixtures Based on the Discrete Element Method

Yuan Gao [1], Guoqiang Liu [1,*] and Nan Jiang [2]

[1] School of Mechanics and Civil Engineering, China University of Mining and Technology, Xuzhou 221116, China; yuangao0708@163.com
[2] Department of Civil & Mineral Engineering, Faculty of Applied Science and Engineering, University of Toronto, Toronto, ON M5S 1A1, Canada; jiangnan.jiang@mail.utoronto.ca
* Correspondence: guoqiangliu@cumt.edu.cn

Abstract: The skeleton structure composed of mineral aggregates is the main body to bear and transfer external loading in asphalt mixtures. To investigate the loading transfer mechanism of the mineral aggregate skeleton, the uniaxial penetration test and Discrete Element Method (DEM) were conducted for the Mineral Aggregate Mixture (MAM) to analyze its mechanical behavior. The three-dimensional strong force chain (SFC) was identified and evaluated based on the proposed recognition criterion and evaluation indices. The results indicate that 4.75 mm should be the boundary to distinguish the coarse and fine aggregates. The skeleton composed of aggregates located on SFCs has better bearing and transferring loading capacity due to its SFC number, average length, and total length decreasing with an increase in the aggregate size. Compared to SMA-16 and OGFC-16, AC-16 exhibits a higher number and total length of its SFC, a smaller average length of its SFC, and a lower average strength of its SFC. Consequently, AC-16 has a lower bearing and transferring loading capacity than that of SMA-16 and OGFC-16. In addition, approximately 90% of SFCs can only transfer external loading downward through 3–5 aggregates. The average direction angle of the SFC formed by fine aggregates is significantly higher than those formed by coarse aggregates. This indicates that the load transfer range of MAM composed of fine aggregates is noticeably larger, leading to lower loading transfer efficiency.

Keywords: three-dimensional strong force chains; mineral aggregate mixtures; recognition criterion; evaluation indices; discrete element method (DEM)

Citation: Gao, Y.; Liu, G.; Jiang, N. Characterization of Three-Dimensional Strong Force Chain Properties of Mineral Aggregate Mixtures Based on the Discrete Element Method. *Buildings* **2024**, *14*, 3289. https://doi.org/10.3390/buildings14103289

Academic Editor: Grzegorz Ludwik Golewski

Received: 5 September 2024
Revised: 26 September 2024
Accepted: 11 October 2024
Published: 17 October 2024

1. Introduction

In asphalt mixtures, the skeleton composed of an MAM serves as the main body to transfer and bear the external loading [1]. To enhance the mechanical properties of the skeleton, various design methods of skeleton-type gradation have been proposed [2]. However, these volume-based mineral aggregate gradation design methods cannot correlate the aggregate gradation and the loading transfer capacity of the mineral aggregate skeleton [3]. Therefore, the mechanical properties of the skeleton have always been the focus of attention in the road field.

To evaluate the mechanical properties of the skeleton of an asphalt mixture, many kinds of methods were proposed. Guo et al. [4] analyzed the movement of coarse aggregates during the formation process of the asphalt mixture skeleton, and the results show that the skeleton stability state is significantly related to the rotations of coarse aggregates. Wang et al. [5] developed a penetration test to analyze the mechanical behavior of porous asphalt mixtures and found that the skeleton strength decreases with the increment of percent passing of 2.36 mm. Sun et al. [6,7] analyzed the deformation behavior of a dense-graded asphalt mixture skeleton based on the interface contact-slip test. The slip deformation of the

skeleton can be divided into five stages, and the skeleton instability is always due to shear failure. In addition to the experimental methods, there are numerical simulation techniques to reveal the mechanical mechanism of the skeleton from the mesoscale perspective. Ma, et al. [8] conducted virtual rutting experiments on asphalt mixtures based on the DEM and concluded that densification in the load-bearing area and lateral movement of aggregates near the load-bearing area are the main causes of rutting. Ding et al. [9,10] proposed a new method to assemble the DEM model of the MAMs and concluded that the thicker coarse aggregate skeleton has a higher proportion of high contact force between different coarse aggregates. Wang et al. [11] investigated the distribution and evolution of contact numbers and contact forces of different gradation MAMs during compaction using DEM, finding that aggregates larger than 4.75 mm contribute significantly to the load-bearing capacity of MAMs. Cai et al. [12] identified the stress transfer in the asphalt mixture skeleton based on the finite element method and indicated that the stress transfer paths are closely linked to the mixture gradation. The above studies demonstrate that it is feasible to investigate the micromechanical behavior of the MAM skeleton via DEM, and the statistical analysis of the contact force can provide insights into the mechanical contribution of different aggregates to the skeleton to some extent. However, it still difficult to deeply reveal the loading transfer mechanism of the mineral aggregate skeleton.

In an asphalt mixture, the mass proportion of MAM is more than 90%. Hence, the asphalt mixture can be seen as the granular material, and other researchers started to analyze the loading transfer capacity of the skeleton based on the granular material mechanics. Chang et al. [13,14] used DEM to construct asphalt mixture two-dimensional models to analyze the evolution of force chains and found that the difference in force chain characteristics between AC-13 and SMA-13 is significant; the force chain theory can be used to evaluate the loading transfer capacity of the skeleton. Shi et al. [15,16] considered the aggregate contact, contact chain, and skeleton as the multiscale structure in the asphalt mixture, and the contact chain can be used to correlate the aggregate contact state and the mechanical properties of the skeleton. Jin et al. [17,18] obtained the contact structure of asphalt mixtures using X-ray CT to identify contact chains. Subsequently, they established evaluation indices for initial skeleton morphology characteristics and morphological evolution characteristics of skeletons. Liu et al. [19] analyzed the force chain recognition criterion for an asphalt mixture skeleton based on the two-dimensional DEM models, and the results indicate that the average normal contact force and 45o need to be set as the force and angle threshold values, respectively. And then, Liu et al. [20,21] established the index system to evaluate the two-dimensional force chain characteristics of the skeleton and found that the skeleton-type asphalt mixtures make it easier to form long force chains for transferring external loading.

The aforementioned studies indicate that the characteristics of force chains are highly correlated with the mechanical properties of mineral aggregate skeletons. Force chains serve as effective tools for studying the structure of MAMs. However, currently, there is no unified criterion for identifying force chains. Some force chain studies are essentially based on the premise of identifying geometric contact chains, and a large number of studies are conducted based on simplified two-dimensional research. Therefore, this study will use the DEM to propose three-dimensional strong force chain (SFC) recognition criterion and identification algorithms to accurately identify the SFC structures in different MAMs to evaluate the characteristics of SFC structures for revealing the loading transfer mechanism of mineral aggregate skeletons.

2. Objective and Scope

The objectives of this study are to accurately identify SFC structures in different MAMs by proposing three-dimensional SFC recognition criterion and algorithms, and to explore the load transfer mechanism of mineral skeletons. To achieve this goal, the three main elements are the following:

(1) To establish three-dimensional DEM models of MAMs with different single-particle sizes and different aggregate gradations, conduct uniaxial penetration tests via PFC3D

software, and calibrate the mesoscopic parameters of the DEM models according to the corresponding laboratory test results;

(2) Based on the existing two-dimensional force chain recognition criteria, the aim is to propose the three-dimensional SFC recognition criterion for MAMs and establish an SFC recognition algorithm;

(3) To establish quantitative evaluation indexes for the geometric and mechanical properties of SFCs, evaluate the characteristics of the SFC structure among different MAMs, and analyze the correlation between the SFC structure and the loading capacity of mineral skeletons.

3. DEM Models and Micromechanical Parameters of MAM

3.1. DEM Models Assembly of MAM

To obtain the micromechanical information of an MAM under external loading, the virtual uniaxial penetration tests of different MAMs were conducted via the three-dimensional particle flow code (PFC3D). In the DEM model, the mineral aggregates were simulated via ball elements, and the steel cylinder and penetration head were all simulated with wall elements. In this study, 4.75 mm was set as the boundary sieve size between coarse and fine aggregates, and the aggregates with a diameter less than 4.75 mm are considered as the fine aggregates. Indoor test results indicated that fine aggregates contribute less to the mineral aggregate skeleton. Therefore, particles within the range of 2.36–4.75 mm diameter were used to represent fine aggregates in the DEM models to balance the computational efficiency.

Dense-graded asphalt concrete, stone mastic asphalt, and open-graded friction course were widely used as the pavement surface layers; therefore, the MAM formed by the median value of the mineral grade of AC-16, SMA-16, and OGFC-16 is selected as the research object. These gradations were determined to establish DEM models via the Chinese standard (JTG F40-2004) [22]. The aggregate gradations are indicated in Figure 1.

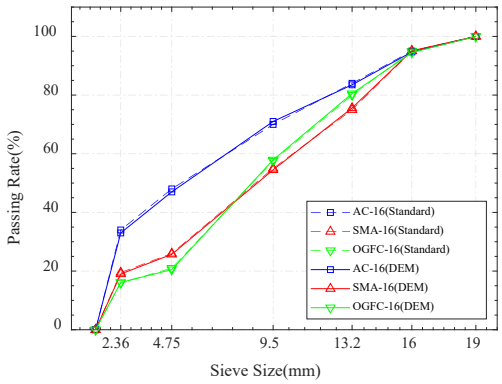

Figure 1. Gradation curves of different MAM.

The assembly of the DEM model is shown as follows. The parts of the DEM models are listed in Figure 2.

1. Calculate the number of balls.

In the DEM model, the MAM is simulated via balls with different diameters. Since the ball is a uniform sphere with a regular shape, its volume can be calculated according to the radius of the ball, and then its mass can be calculated after artificially giving its density. Then, the number of balls that need to be generated to simulate the specified particle size in the DEM model can be calculated using Equation (1).

$$N_{pi} = \frac{m_i \cdot P_i}{\frac{4}{3} \times \pi \times [(r_{\max} + r_{\min})/2]^3 \times \rho_m} \quad (1)$$

where N_{pi} represents the number of balls required to simulate the i-th level of material in the MAM; P_i indicates the mass fraction of the i-th level material in the MAM. m_i denotes the mass of the DEM specimen of the MAM which is 3 kg in this study. $r_{\max}$ and $r_{\min}$ indicate the maximum and minimum radii of particles within the current particle size range, respectively. ρ_m denotes the apparent density of the material, measured in the laboratory as $\rho_m = 2775.57 \mathrm{KN/m^3}$;

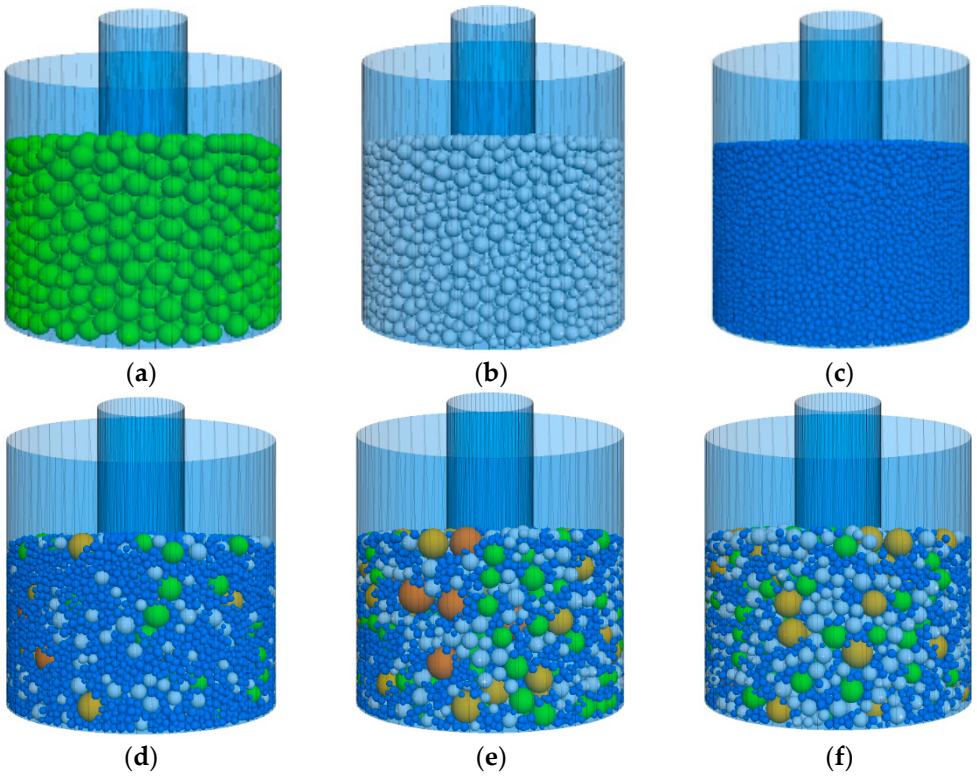

Figure 2. Different DEM specimens of MAMs: (**a**) 9.50–13.2 mm; (**b**) 4.75–9.50 mm; (**c**) 2.36–4.75 mm (**d**) AC-16; (**e**) SMA-16; (**f**) OGFC-16.

2. Assemble DEM model.

Create a sealed cylindrical wall with a diameter of 152 mm. Then, generation all of balls inside the space surrounded by walls, and applying gravitational acceleration to the Balls for free-fall motion. And then, applying a cyclic velocity in the xyz directions to the wall for shaking the balls;

3. Preload DEM model.

Remove the excess walls, leaving only one open cylindrical wall with a diameter of 152 mm and a height of 150 mm. Subsequently, generate a disk with a diameter of 152 mm to apply a constant preloading force to the DEM specimen at a rate of 1.25 mm/min until the preload force reaches 10 KN;

4. Prepare to insert DEM model.

Raise the preloading disk with a speed of 0.125 mm/min until the top surface of the DEM specimen reaches the initial stress-free state; then, remove the simulated preloading disk wall. And then, generate a cylindrical wall with a diameter of 50 mm to simulate the penetration head, and slowly lower it until it makes contact with the MAM.

3.2. Micromechanical Contact Models and Parameters of DEM Models for MAM

3.2.1. Micromechanical Contact Models

The accurate micromechanical contact models and their parameters are important preconditions for obtaining correct results in DEM simulations of MAMs. In previous

studies, the parallel bond model [23,24] or Burger's model [25,26] was always used to analyze the mechanical behavior of asphalt mixtures based on DEM. The parallel bond model can be decomposed into the linear contact model and bond model, and the bond model is assigned to simulate the adhesive action of an asphalt binder. In this study, the MAM is the research object, and the contact models need to describe two types of contacts (Ball–Ball, Ball–Wall). Balls and walls, respectively, simulate the mineral aggregates and the steel experimental apparatus, both of which can be considered rigid elements. Therefore, the micromechanical contact models are all set as linear contact models in this study [27]. The linear contact model is illustrated in Figure 3.

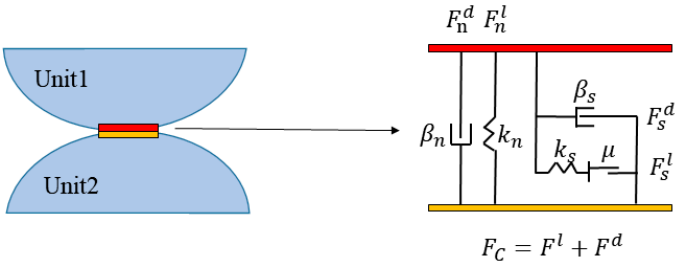

Figure 3. Schematic diagram of linear contact model.

As shown in Figure 3, the contact interface set via the linear contact model is an infinitesimal interface that transmits only contact forces without transmitting moments. The contact force F_C can be decomposed into the linear contact force F^l and damping force F^d, both of which can be further decomposed into the normal force F_n and tangential force F_s. The linear force is generated via linear springs with constant normal and shear stiffness, while the damping force is generated via viscous dampers. In the DEM simulation process, the dampers gradually absorb the kinetic energy of the system to allow it to reach equilibrium. In this study, local damping is set to 0.7.

The formula for calculating the normal linear force F_n^l is given by Equation (2).

$$F_n^l = k_n u_n \tag{2}$$

where k_n represents the normal stiffness at contact, and u_n represents the normal overlap between discrete elements.

The formula for calculating the tangential linear force F_s^l is given by Equations (3)–(5).

$$F_s^* = \left(F_s^l\right)_0 - k_s \Delta u_s \tag{3}$$

$$F_s^\mu = \mu F_n^l \tag{4}$$

$$F_s^l = \begin{cases} F_s^*, \|F_s^*\| \le F_s^\mu \\ F_s^\mu \cdot \left(\frac{F_s^*}{\|F_s^*\|}\right), else \end{cases} \tag{5}$$

where k_s represents the tangential stiffness at contact; $\left(F_s^l\right)_0$ represents the initial tangential linear force at the beginning of a contact at a certain time step; Δu_s represents the relative tangential displacement generated between two contacting solid elements within one time step; μ represents the friction coefficient at contact inception.

For the tangential linear force F_s^l, PFC3D uses the incremental method to update it in real time. When the relative displacement between two contacting solid elements within one time step is Δu_s, the increment of the tangential linear force F_s^l is $k_s \Delta u_s$. The upper limit of the tangential linear force is determined by the friction coefficient μ and the normal linear force F_n^l.

Based on the property inheritance method, this study sets the k_n, k_s, and μ parameters for the ball and wall entities. This approach involves assigning distinct microscale properties to different types of entities in the DEM simulation. When contact occurs between

two different entity types, the microscale parameters at the contact interface are calculated based on Equations (6)–(8).

$$k_n = \frac{k_n^{(1)} \cdot k_n^{(2)}}{k_n^{(1)} + k_n^{(2)}} \tag{6}$$

$$k_s = \frac{k_s^{(1)} \cdot k_s^{(2)}}{k_s^{(1)} + k_s^{(2)}} \tag{7}$$

$$\mu = \min(\mu^{(1)}, \mu^{(2)}) \tag{8}$$

3.2.2. Micromechanical Contact Models

In this study, the mineral aggregates, with the same material and sourced from the same batch of quarried stones, were all black basalt. The mineral aggregates were divided into 12 gradations based on their particle size range, and part of the specimens are shown in Figure 4.

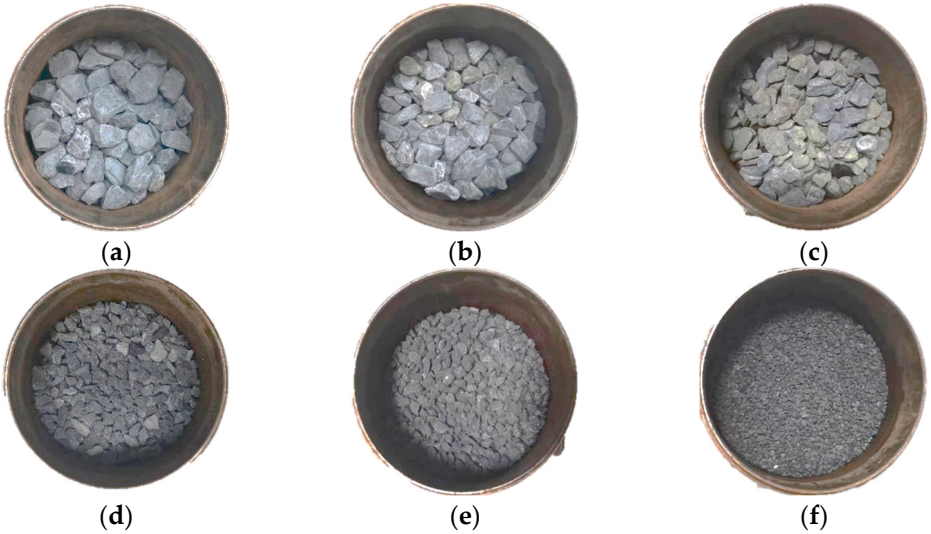

Figure 4. Different single-sized MAMs: (**a**) 19.0–26.5 mm; (**b**) 16.0–19.0 mm; (**c**) 13.2–16.0 mm (**d**) 9.50–13.2 mm; (**e**) 4.75–9.50 mm; (**f**) 2.36–4.75 mm.

Referring to the California Bearing Ratio (CBR) test [28] and the uniaxial penetration test of asphalt mixtures [29], a uniaxial penetration test was designed for the MAMs. Because the MAMs lack an asphalt binder, a steel mold is necessary to confine the aggregates during the processes of specimen preparation and testing. A steel penetration head was used to penetrate the MAMs, and the test instrument is shown in Figure 5.

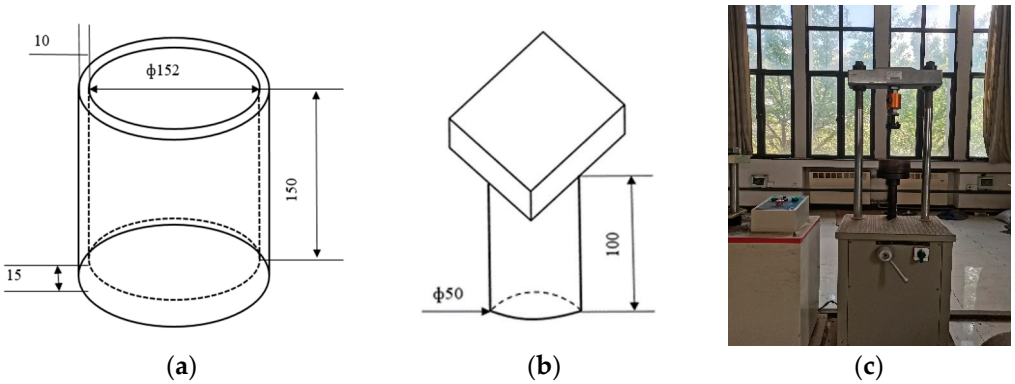

Figure 5. Experimental instruments: (**a**) test cylinder size diagram; (**b**) penetration head; (**c**) pavement strength tester, which can load the specimen at a constant speed of 1.25 mm/min.

In this study, each specimen contains 3 kg of single-sized MAMs (SMAMs). These SMAMs were poured into the steel mold and leveled. And then, a metal disc with the same diameter of the steel mold was attached to the surface of the SMAM specimen. The specimen was then placed in a hydraulic press and preloaded at a constant rate of 1.25 mm/min until the preload force reached 10 KN. During the molding process, the SMAM composed of aggregates smaller than 0.075 mm was excessively loose and could not be compacted into shape. Hence, uniaxial penetration tests for the SMAM with aggregates smaller than 0.075 mm were abandoned. The uniaxial penetration tests were conducted using the pavement strength tester. The penetration rod is slowly inserted until it just touches the surface of the MAM, at which point this state is designated as the starting point of loading. In this study, the penetration speed of the plunger is set at 1.25 mm/min. The SMAM specimen is then penetrated for a duration of 20 min, reaching a depth of 25 mm. The test results are listed in Figure 6.

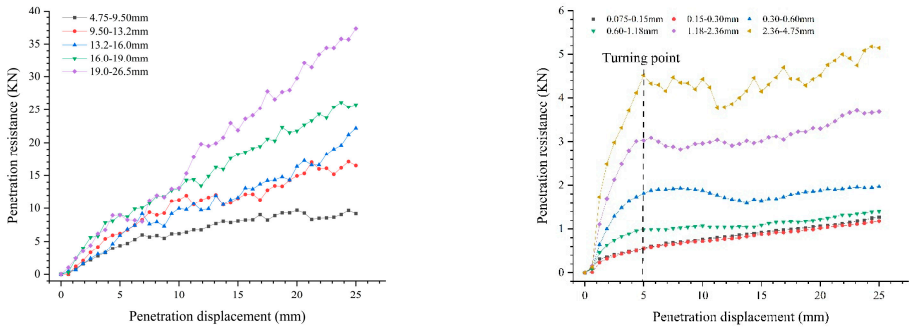

(**a**) (**b**)

Figure 6. Penetration resistance curve of SMAMs: (**a**) coarse aggregates; (**b**) fine aggregates.

As shown in Figure 6, the penetration resistance of the SMAM with particle sizes larger than 4.75 mm increases linearly with the increase in penetration depth during the penetration process. However, the penetration resistance curve of the SMAM with particle sizes smaller than 4.75 mm shows a significant inflection point at a penetration depth of 5 mm. Below a penetration depth of 5 mm, the penetration resistance steadily increases, but after a penetration depth of 5 mm, the penetration resistance basically stops increasing. This phenomenon shows that compared with fine aggregates, coarse aggregates can interlock with each other to form a stable aggregate skeleton, so MAMs formed from coarse aggregates can provide stable linear growth resistance.

3.2.3. Micromechanical Parameters

This study calibrated the microscale parameters of the virtual specimens based on the previously obtained penetration resistance curves of SMAM in the laboratory and the virtual penetration resistance curves obtained in the DEM simulation. The correlation between the two curves was verified using the Pearson correlation analysis method. According to previous studies, $\mu = 0.4$ is a reasonable value for mineral material [23,30]. The k_n and k_s of the wall and different particle size ranges of the ball were continuously adjusted. When the correlation coefficient $r > 0.95$, the microscale parameters at this point were set as the parameters for DEM simulation in this study.

The formula for calculating the Pearson correlation coefficient can be found in Equation (9).

$$r = \frac{\sum (x_r - x_s)(y_r - y_s)}{\sqrt{\sum (x_r - x_s)^2} \sqrt{\sum (y_r - y_s)^2}} \quad (9)$$

The microscale parameters of the wall and the simulated balls of different particle sizes, along with their correlation coefficients, are presented in Table 1.

Table 1. Micromechanical parameters of DEM contact models.

Cell Type	Particle Size (mm)	Mesoscopic Parameter k_n(N/m)	Mesoscopic Parameter k_s(N/m)	μ	Correlation Coefficient
Wall	—	5.00×10^{11}	5.00×10^{11}	0.4	—
Ball	19.0–26.5 mm	6.50×10^{6}	6.50×10^{6}	0.4	0.99066
	16.0–19.0 mm	4.50×10^{6}	4.50×10^{6}	0.4	0.98537
	13.2–16.0 mm	2.00×10^{6}	2.00×10^{6}	0.4	0.97941
	9.50–13.2 mm	1.25×10^{5}	1.25×10^{5}	0.4	0.98484
	4.75–9.50 mm	3.00×10^{5}	3.00×10^{5}	0.4	0.99039
	2.36–4.75 mm	6.00×10^{4}	6.00×10^{4}	0.4	0.96855

The penetration resistance curves of SMAMs and GMAMs in the DEM specimens are shown in Figure 7, respectively. Under the microscale contact parameters shown in Table 1, the DEM simulation results of SMAMs are in good agreement with the laboratory results, and the DEM simulation results of GMAMs also conform to the patterns observed in previous studies. These observations indicate that the microscale contact model and parameters selected in this study ensure the accuracy of the DEM simulation.

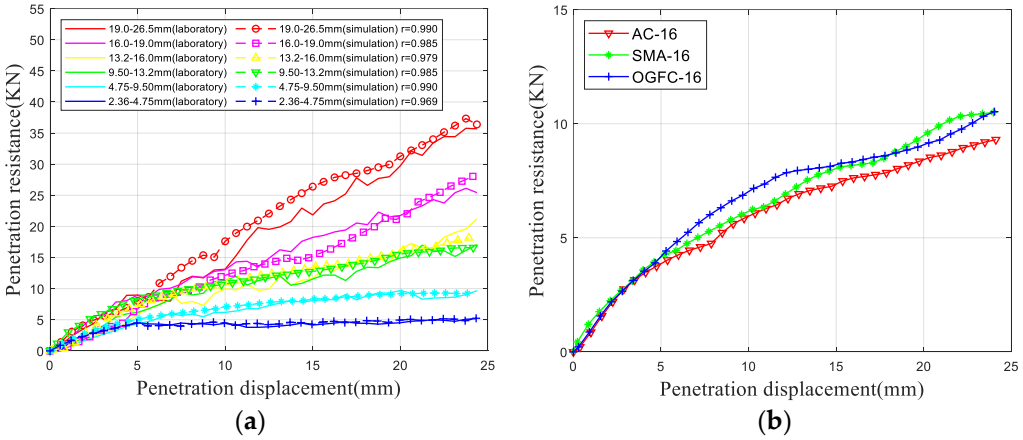

Figure 7. Penetration resistance curve of DEM specimens: (**a**) SMAMs; (**b**) GMAMs.

3.3. Virtual Uniaxial Penetration Test Program

After forming the DEM specimens of the mineral mixture, this study conducted virtual uniaxial penetration experiments similar to indoor uniaxial penetration tests. This study controlled the virtual penetration head to move downward at a constant speed of 1.25 mm/min until a penetration depth of 25 mm was reached; the virtual uniaxial penetration test program is shown in Figure 8. During this process, the virtual penetration resistance curve of the MAM was recorded.

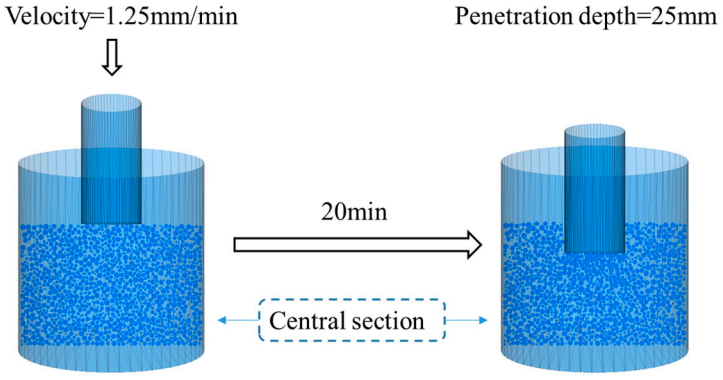

Figure 8. The virtual uniaxial penetration test program.

After the virtual penetration test was completed, this study utilized the built-in Fish compiler in PFC3D to compile programs, traverse the particle information and contact information in the DEM specimens of the MAMs, and export these microscopic details.

4. Recognition Criterion and Evaluation Indices of SFC

4.1. Recognition Criterion and Algorithm

Under external loading, force chains with different strengths will be formed. According to the difference in the forces carried on the force chain, the force chains are divided into strong force chains (SFCs) and weak force chains (WFCs). In a force chains network, the SFC bears and transfers most of the external loading. Hence, the characteristics of SFCs are closely related to the loading transfer capacity of MAMs, and this study focuses on the analysis of SFCs. Referring to the recognition criterion of a two-dimensional force chain for an asphalt mixture skeleton, the recognition criterion of three-dimensional SFCs need to include five aspects, as follows:

(1) Aggregate count threshold: a single SFC needs to consist of at least 3 or more mineral aggregates in an MAM. This ensures that the identified SFC meets the requirements for a chain-like shape;

(2) Normal contact force threshold: according to the previous studies, the contacts between aggregates with greater normal force have a significant contribution to bear and transfer external loading. And so, the average normal contact force of all aggregate contacts is set as the threshold [31]. When the normal contact force is greater than a threshold value, the corresponding aggregate is involved in the forming of an SFC;

(3) Contact angle threshold: according to previous studies, force chains exhibit various forms, including linear, looped, coupled, and more [32]. However, the criteria proposed in this study aim to identify force chains capable of effectively bearing and transmitting loads. Therefore, a contact angle threshold of $\theta_{threshold} = 45°$ was set in this research. This ensures that the identified strong force chains exhibit nearly linear configurations. The schematic diagram of the contact angle threshold is shown in Figure 9;

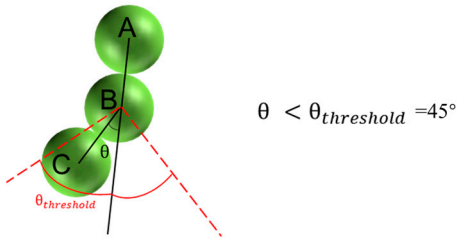

Figure 9. Contact angle threshold.

(4) Downward force transmission criterion: this study stipulates that in the natural coordinate system, starting from the second mineral particle that constitutes a strong force chain, all mineral particles forming the strong force chain must have a Z-coordinate of their center of mass less than that of the preceding mineral particle. This criterion effectively eliminates the occurrence of "crescent-shaped" SFCs, as depicted in Figure 10;

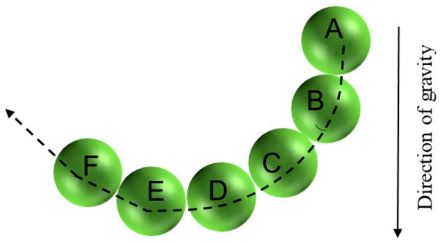

Figure 10. "Crescent-shaped" SFC.

(5) Force extension criterion: when an SFC extends downward and multiple mineral particles within the contact angle threshold are encountered, the particle with the maximum force-extension parameter γ is selected as the SFC particle to continue extending downward. The force-extension criterion effectively addresses the issue of difficulty in determining the extension direction of an SFC when multiple mineral particles are encountered within the contact angle threshold. The formula for the force-extension parameter γ is shown in Equation (10), and its schematic diagram is illustrated in Figure 11.

$$\gamma = f\cos\theta \tag{10}$$

where f represents the normal contact force between particles, and θ represents the contact angle.

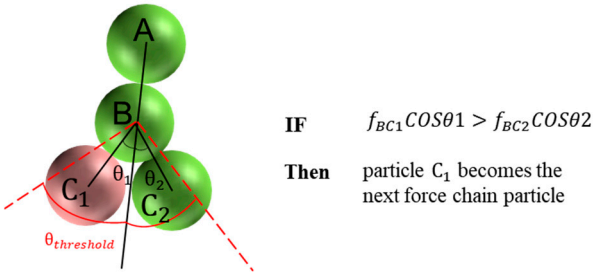

Figure 11. Force-extension γ diagram.

Referring to the recognition criterion of a three-dimensional SFC, the recognition algorithm was proposed, and the algorithm program is illustrated in Figure 12a. There are repeat SFCs identified via the algorithm shown in Figure 12a. To ensure the accuracy of subsequent quantitative analysis of SFC characteristics, a repeat SFC recognition algorithm was proposed to remove duplicate identified SFCs, and its algorithm program is illustrated in Figure 12b.

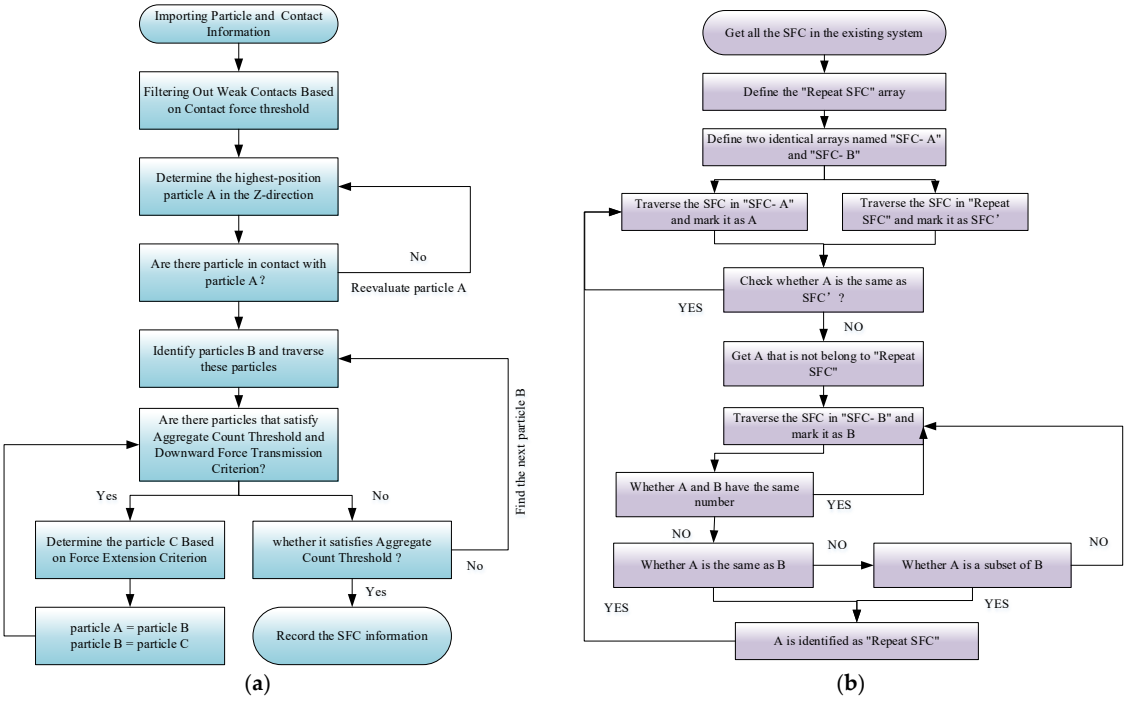

Figure 12. Program of SFC recognition algorithm: (**a**) SFC recognition algorithm; (**b**) repeat SFC recognition algorithm.

Based on the SFC identification algorithm proposed in this study, the strong force chain (SFC) network in the mineral mixture can be successfully identified. Taking the SMAM with an aggregate size range of 2.36–4.75 mm as an example, as shown in Figure 13, the contact network of an MAM can be distinguished into SFC and WFC contact networks, respectively. Correspondingly, the mineral particles can also be classified into SFC and WFC aggregates.

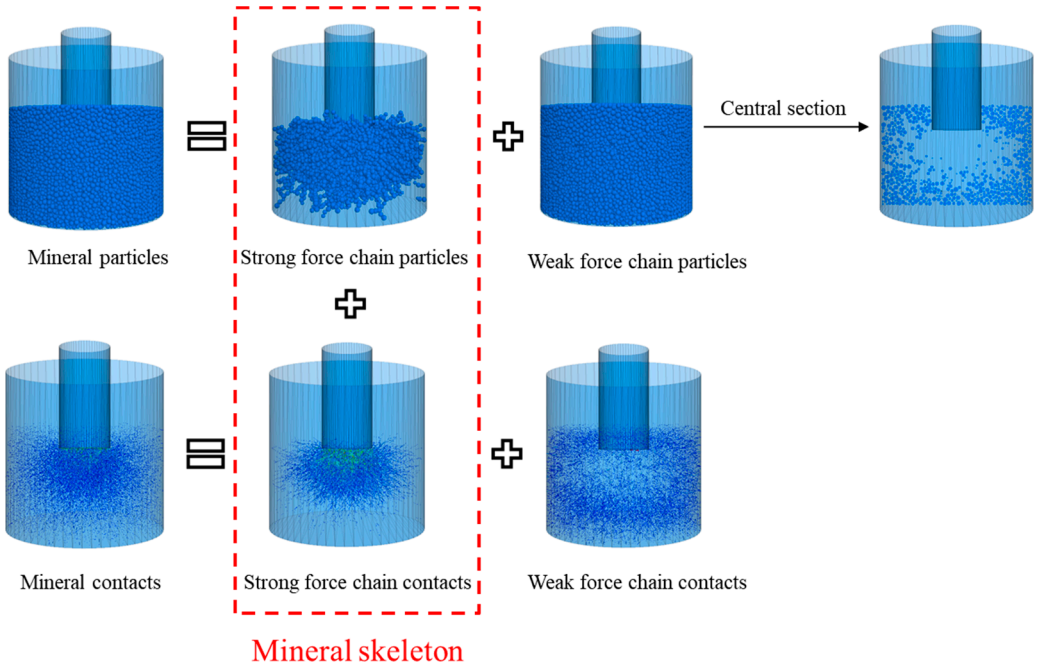

Figure 13. Mineral skeleton diagram of SMAM with 2.36–4.75 mm.

4.2. Recognition Criterion and Algorithm

To characterize the properties of the SFC structure in an MAM quantitatively, various evaluation indices were proposed to represent the morphological and mechanical characteristics of the SFC.

(1) The number of SFCs

According to the force chain recognition criterion proposed in this study, there are significant differences in the number of SFCs within different mineral mixtures. The number of SFCs can reflect the complex network characteristics of the mineral skeleton. The higher the number of SFCs, the greater the complexity of the SFC structure;

(2) The length the SFC

The length of an SFC effectively characterizes its geometric properties. A longer SFC implies a longer path for load transmission, thereby indicating the complexity of the mineral framework network and the efficiency of load transmission. The calculation formula for the length l_i of an SFC is given by Equation (11).

$$l_i = \sum_{j=2}^{N_i-1} d_j + r_1 + r_{N_I} \tag{11}$$

where l_i represents the length of the i-th SFC, N_i denotes the number of particles in the i-th SFC, r_1 signifies the radius of the first particle in the SFC, r_{N_I} indicates the radius of the last particle in the single SFC, and d_j represents the diameter of other SFC particles;

(3) The number of particles in the SFC

The parameter N_i represents the number of mineral particles composing the i-th SFC, indicating the composition characteristics of the SFC;

(4) The linearity of the SFC

The linearity of an SFC is used to evaluate the degree to which a single SFC resembles a straight line. The calculation formula for the linearity L_i of an SFC is given by Equation (12).

$$L_i = 1 - \frac{\sum_{P=1}^{M} \theta_P}{M \times 90} \tag{12}$$

where M refers to the number of contacts in the SFC, M = −1; θ_P denotes the contact angle.

As shown in Figure 14, a higher SFC linearity indicates that the geometric shape of the individual SFC is closer to a straight line, implying greater stability in the structure of the individual SFC and higher efficiency in load transmission. Conversely, a lower SFC linearity suggests that the shape of the individual SFC is closer to a polyline. This type of SFC structure is prone to damage and is less conducive to transmitting external loads;

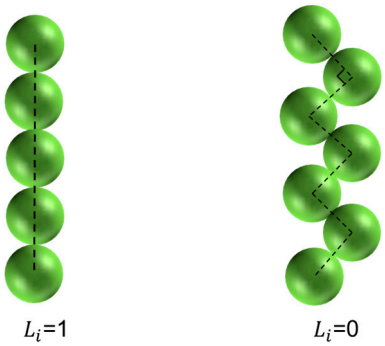

Figure 14. The linearity of SFCs.

(5) The orientation angle of the SFC

This study defines the orientation angle of an SFC as the angle between the direction of the line connecting the centroids of the first and last mineral particles in the SFC and the direction of gravity. The formula for calculating the orientation angle θ_{Angle} of an SFC is shown in Equation (13), and a schematic diagram illustrating the orientation angle of an SFC is depicted in Figure 15.

$$\theta_{Angle} = \arccos\left(\frac{(z_B - z_A)}{\sqrt{(x_B - x_A)^2 + (y_B - y_A)^2 + (z_B - z_A)^2}}\right) \tag{13}$$

where (x_A, y_A, z_A) refers to the position coordinates of the first particle in the SFC; (x_B, y_B, z_B) refers to the position coordinates of the last particle in the SFC;

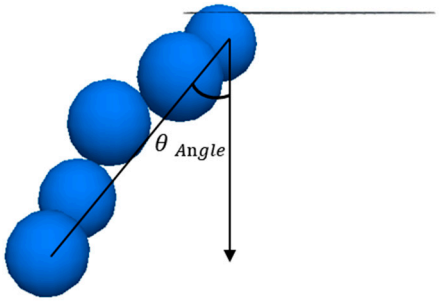

Figure 15. The orientation angle of an SFC.

(6) The strength of the SFC

This study defines the strength of an SFC as the sum of all contact forces on the SFC; it characterizes the magnitude of the load borne by a single SFC. The formula for calculating the strength p_i of an SFC is shown in Equation (14).

$$p_i = \sum_{P=1}^{M} f_p \tag{14}$$

where f_p represents the contact force on the SFC; M represents the total number of contacts on the i-th SFC.

5. Results and Discussions

5.1. Single-Particle Size of MAM

The aggregates and contacts identified based on the recognition criterion of SFCs play a dominant role in bearing and transferring external loading. The contribution of particles and contacts located in WFCs can be negligible. Therefore, these aggregates and contacts located in the SFC can be regarded as forming the skeleton of the MAM. The SFC of a single-particle size MAM is identified using the above algorithm, and the aggregates located on the SFC are shown in Figure 16.

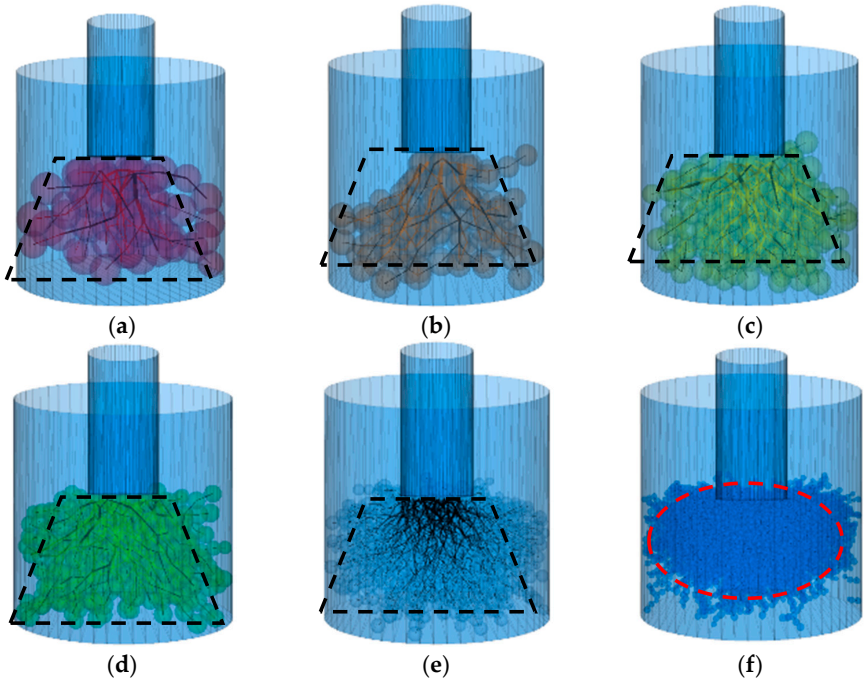

Figure 16. Identified aggregates located on SFC of SMAMs: (**a**) 19.0–26.5 mm; (**b**) 16.0–19.0 mm; (**c**) 13.2–16.0 mm (**d**) 9.50–13.2 mm; (**e**) 4.75–9.50 mm; (**f**) 2.36–4.75 mm.

It can be seen from Figure 16 that when the aggregate size of the aggregate exceeds 4.75 mm, the structure of the mineral skeleton of the SMAM appears as a "narrow top and wide bottom" circular cone shape. This phenomenon indicates that when the MAM composed of coarse aggregates withstands external loads from the penetrating head, the load is transmitted downward through the SFC until it reaches the bottom of the MAM. When the particle size of the aggregate is less than 4.75 mm, the mineral skeleton of the MAM composed of fine aggregates appears as an ellipse around the penetrating head. This indicates that when the mineral mixture composed of fine aggregates withstands loads, only the aggregates near the load-bearing area are compressed and resist external loads. Therefore, the mineral skeleton of the mineral mixture composed of fine aggregates cannot transmit the load to the bottom or the next layer. This is also the microscopic mechanical

reason for the obvious inflection point in the penetration resistance curve of the MAM composed of fine aggregates.

The SFC characteristics for different SMAMs are presented in Figure 17.

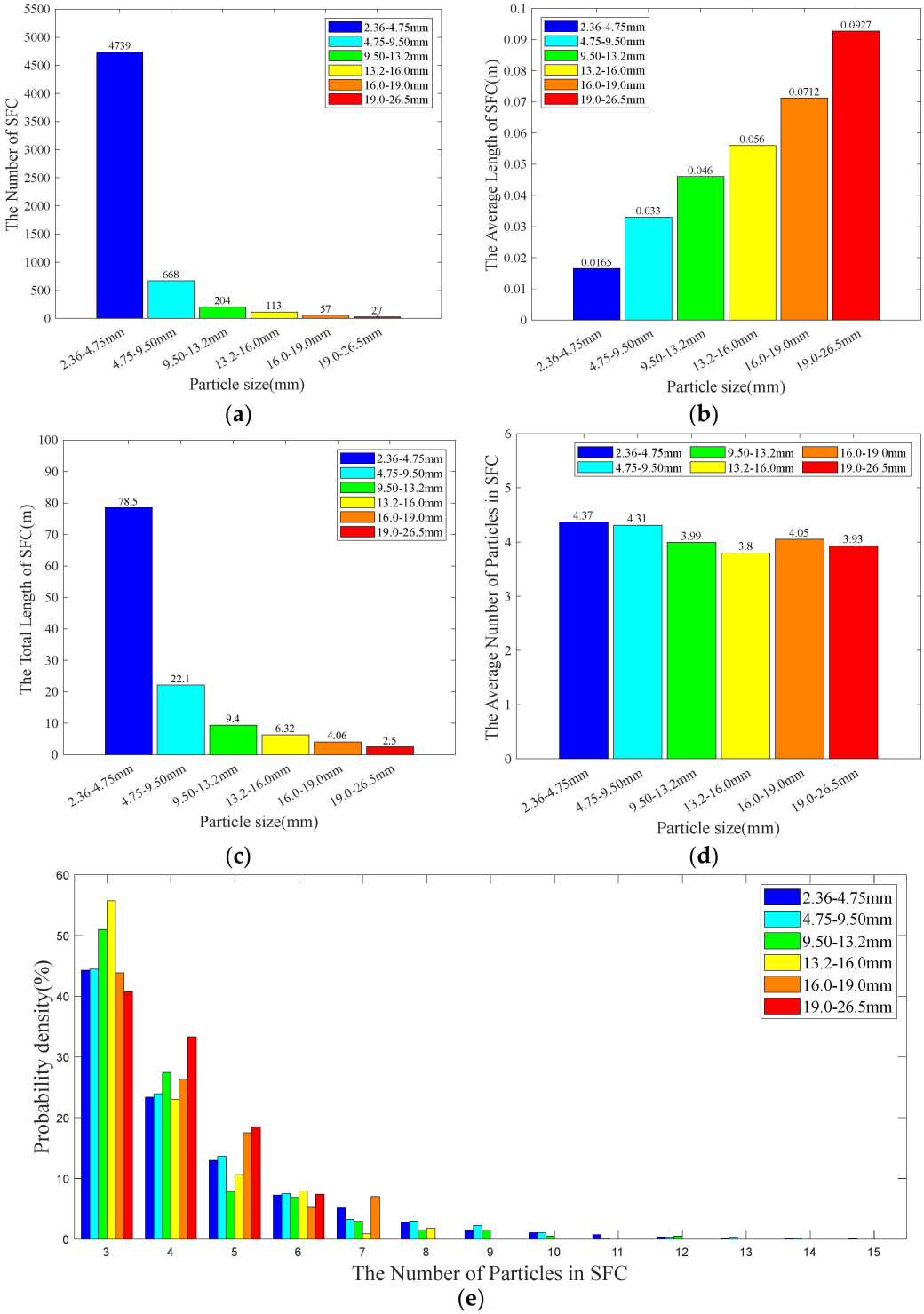

Figure 17. *Cont.*

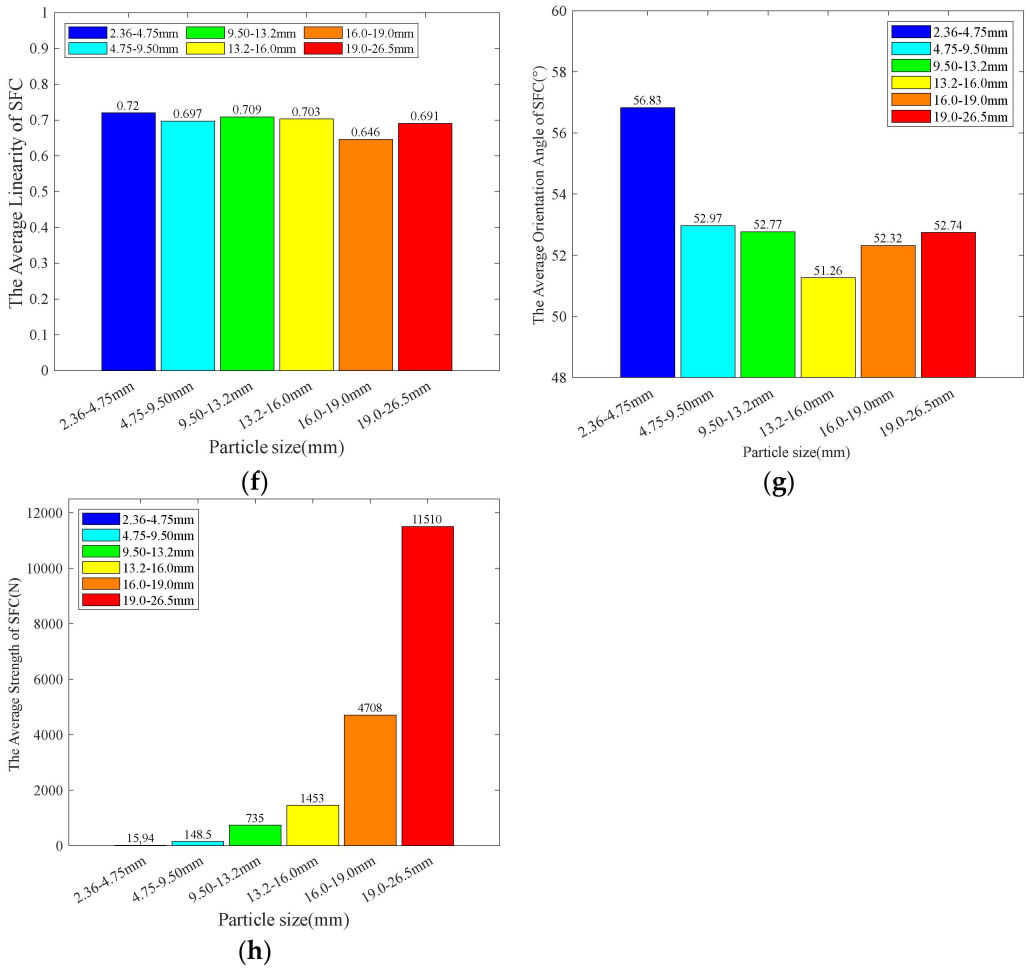

Figure 17. SFC characteristics of SMAMs: (**a**) the number of SFCs; (**b**) the average length of the SFCs; (**c**) the total length of the SFCs; (**d**) the average particle number in an SFC; (**e**) particle number distribution; (**f**) the average linearity; (**g**) the average orientation angle; (**h**) the average strength.

It can be seen from Figure 17a that the number of SFCs decreases with an increase in the aggregate size of the SMAM under the same conditions. The number of SFCs in different mineral mixtures reflects the complex network characteristics of the mineral skeleton. Therefore, the above phenomenon indicates that the complexity of the SFC structure in an SMAM decreases with the increasing aggregate size of the SMAM. For the length distribution of SFCs in an SMAM, the data in Figure 17b show that the average length of SFCs increases with an increase in aggregate size, while the data in Figure 17c show that the total length of SFCs decreases with the aggregate size increasing. These observations suggest that the individual SFCs tend to have longer lengths as the aggregate size increases.

It can also be seen from Figure 17d that the average number of particles of SFCs is around four in different SMAMs, and the SFC has slightly higher average particle counts in SMAMs with smaller particle sizes. From Figure 17e, it can be observed that for any SMAM, the majority of SFC particle counts fall within the range of 3 to 5, with SFCs composed of six or more aggregates accounting for only about 10%. Additionally, the maximum number of particles in an SFC decreases as the aggregate size increases. This phenomenon indicates a limitation in the extension capability of SFCs in mineral mixtures, where most SFCs can only transfer external loading downwards through three to five aggregates, and the trend is unaffected by the aggregate size.

The average linearity and probability distribution/cumulative curves of SFCs for different SMAMs are presented in Figure 17f; the average linearity of SFCs for different

SMAMs is around 0.7. These observations indicate that most SFCs in SMAMs exhibit good straight-line characteristics, and the linearity of SFCs is not significantly influenced by the aggregate size. SFCs with a larger orientation angle indicate a smaller proportion of load transferred downwards, thus implying the SFC with the lower load transfer efficiency. The data in Figure 17g show that the average orientation angles of SFCs is between 50° and 60°. Moreover, the average orientation angle of SFCs composed of fines (2.36–4.75 mm particle size range) is notably higher than those composed of coarse aggregates. These results suggest that SFCs are formed with angles ranging from 0° to 90° concerning the gravity direction under external loading, facilitating the downward and lateral transmission of external loading. And the external loading transfer efficiency of SFCs in fines-based mineral mixtures is lower than that of coarse aggregate-based mineral mixtures. SFC strength characterizes the ability of an SFC to bear and transfer external loadings; an SFC with higher strength indicates a greater capacity for bearing and transferring external loading. The data in Figure 17h show that there is a significant difference between the average strength of SFCs for different SMAMs. The SFC strength noticeably increases with an increase in aggregate size. These findings suggest that the larger mineral aggregate size can result in forming SFCs with higher strength. Therefore, the larger mineral aggregate size can enhance the load-bearing capacity of the MAM.

5.2. Graded MAMs

The SFCs of GMAMs are also identified using the above algorithm, and the aggregates located on the SFC are shown in Figure 18.

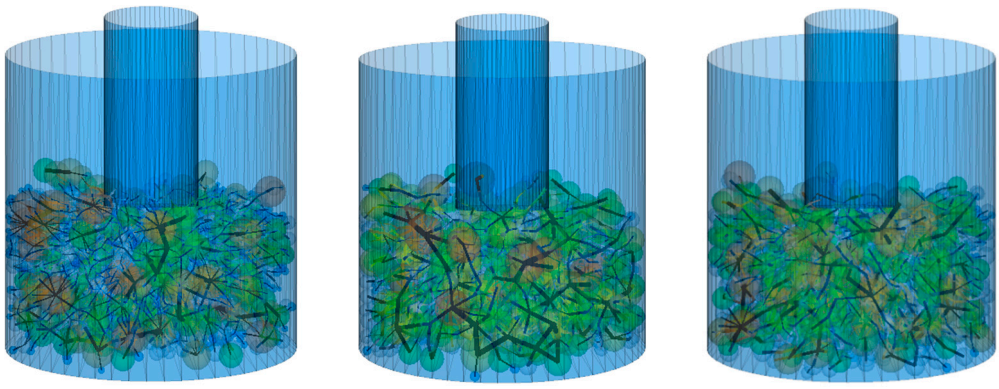

Figure 18. Identified aggregates located on SFCs of different GMAMs: (**a**) AC-16; (**b**) SMA-16; (**c**) OGFC-16.

The number of SFCs in DEM specimens of AC-16, SMA-16, and OGFC-16 is 2717, 1409, and 1251, respectively; the number of SFCs of AC-16 is approximately twice that of SMA-16, while the number of SFCs of OGFC-16 is slightly lower than SMA-16. This result shows that the skeleton of AC-16 exhibits higher complexity compared to SMA-16 and OGFC-16. The phenomenon indicates that the loading transfer efficiency of the skeleton of AC-16 is significantly lower than that of the other two GMAMs.

It can also be seen from Figure 19 that the average length of the SFCs of AC-16 is significantly lower than that of SMA-16 and OGFC-16. However, the total length of the SFC of AC-16 is higher than that of the other two GMAMs. It can be seen from Figure 19c that the proportion of SFCs with a shorter length for AC-16 is significantly higher than that of the other two GMAMs. This result indicates that the SFC lengths in AC-16 mixtures are generally shorter than the other two GMAMs, implying that the individual load transfer paths of SFCs in AC-16 are shorter compared to SMA-16 and OGFC-16. However, the total load transfer path of the entire mineral skeleton in AC-16 is longer. This result suggests that the load transfer efficiency of AC-16 is significantly lower than that of the other two GMAMs.

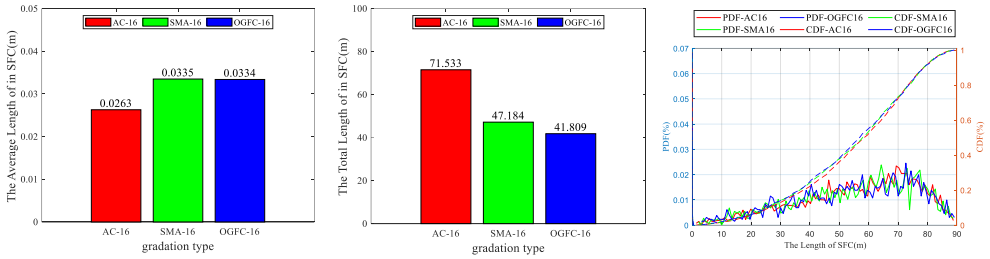

(**a**) (**b**) (**c**)

Figure 19. The length of the SFC of different GMAMs: (**a**) the average length of the SFC; (**b**) the total length of the SFC; (**c**) the length distribution of SFC.

As shown in Figure 20, the probability distribution of the number of particles in SFCs for different GMAMs exhibits a similar trend, with nearly 90% of SFC particle numbers falling between three and five. The average number of particles in SFCs for AC-16 is notably lower than SMA-16 and OGFC-16. Additionally, the maximum SFC particle number for AC-16 is significantly higher than the other two GMAMs. This result indicates that there are limitations in the extension capability of SFCs in GMAMs. Most SFCs can only transfer external loading downwards through 3–5 aggregates, and this trend is not influenced by the gradation type.

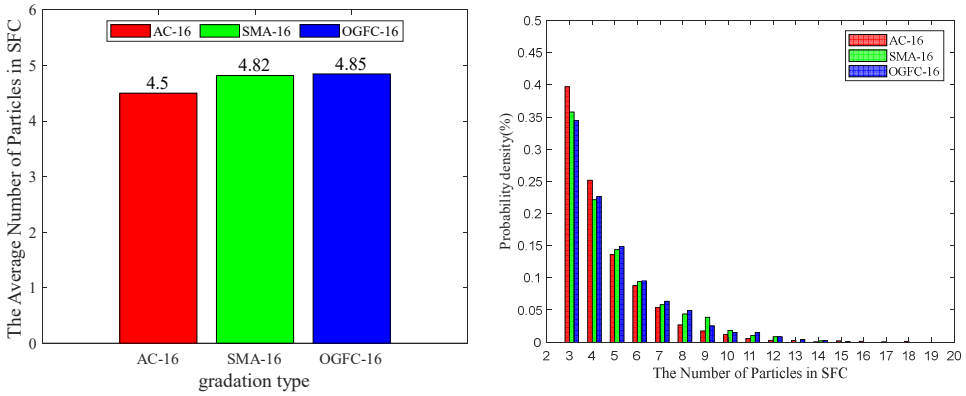

(**a**) (**b**)

Figure 20. The number of particles in SFCs of different GMAMs: (**a**) average particle number in an SFC; (**b**) particle number distribution in SFCs.

It can be clearly observed from Figure 21 that the distribution of the linearity of SFCs is similar for different GMAMs, and almost all the linearity values of SFCs are greater than 0.5. Additionally, the average linearity of SFCs in AC-16 is notably higher than that of SMA-16 and OGFC-16, and the proportion of SFCs with poor linearity in AC-16 is significantly lower than that of SMA-16 and OGFC-16. This result indicates that AC-16 can generate a higher proportion of SFCs with good linearity due to the shorter length.

The average orientation angle of SFCs for different GMAMs are almost the same, and the distribution of SFC direction angles is very similar, as shown in Figure 22. This result indicates that the distribution of the orientation angle of SFCs is almost identical in different GMAMs under the same load-bearing conditions, and the diffusion range of load transfer in the skeleton of different GMAMs is nearly the same.

The average strength of SFCs and the distribution of the strength of SFCs of different GMAMs are presented in Figure 23. The result shows that the average strength of SFCs for SMA-16 is more than twice that of AC-16, while the average strength of SFCs in OGFC-16 is slightly higher than SMA-16. Meanwhile, the proportion of SFCs with lower strength in AC-16 is significantly higher than that of SMA-16 and OGFC-16. This indicates that the load-bearing capacity of AC-16 is generally lower than that of SMA-16, and OGFC-16 has the largest load-bearing capacity.

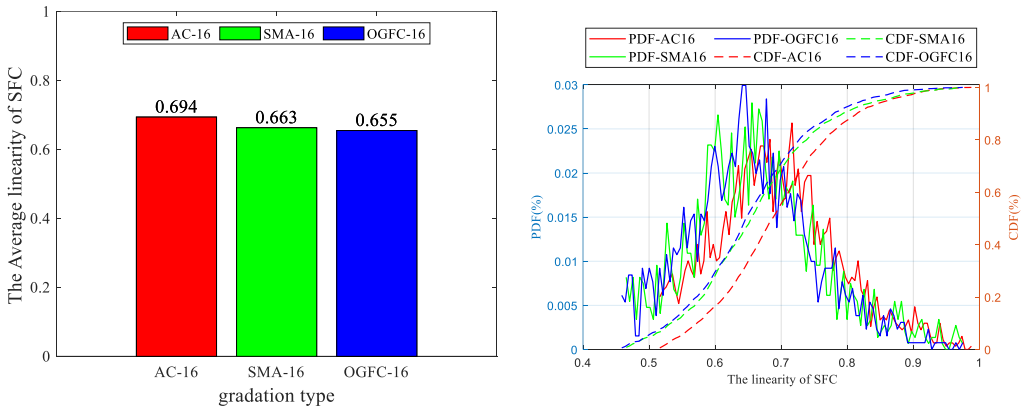

(**a**) (**b**)

Figure 21. The linearity of SFCs of different GMAMs: (**a**) the average linearity of SFCs; (**b**) the linearity distribution of SFCs.

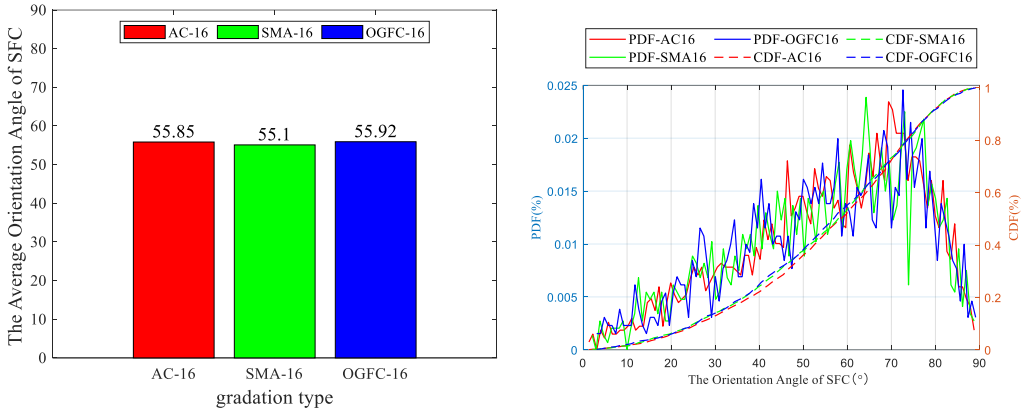

(**a**) (**b**)

Figure 22. The orientation angle of SFCs of different GMAMs: (**a**) the average orientation angle of SFCs; (**b**) the orientation angle distribution of SFCs.

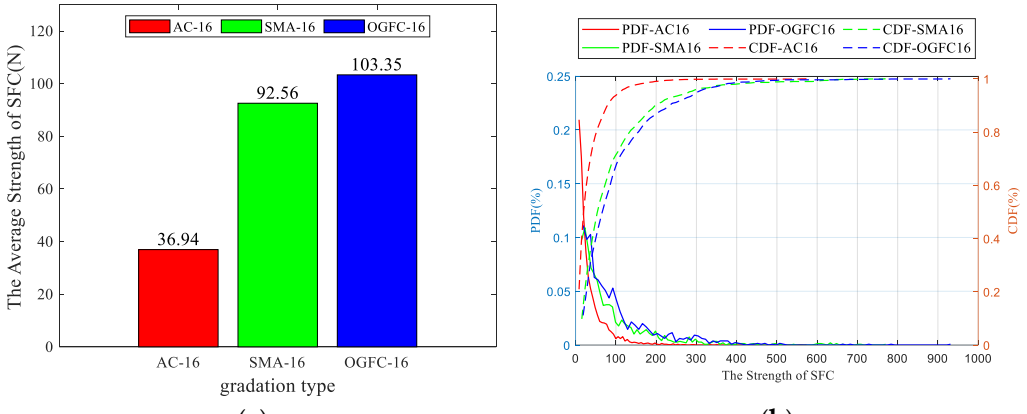

(**a**) (**b**)

Figure 23. The strength of SFCs of different GMAMs: (**a**) the average strength of SFCs; (**b**) the strength distribution of SFCs.

6. Conclusions

This study conducted uniaxial penetration experiments and DEM simulations on different MAMs and proposed the recognition criteria and evaluation indices to identify and evaluate three-dimensional strong force chains. Based on the aforementioned results and discussions, the following conclusions can be drawn:

(1) The MAM formed by small particle size aggregate particles cannot form a stable mineral skeleton to effectively resist external load, while the MAM composed of a higher proportion of coarse aggregate can effectively improve the stability of the MAM, thereby increasing the strength of the mineral skeleton;
(2) The SFC number, average length, and total length decrease with an increase in the aggregate size, while the average strength of SFC increases with the aggregate size increasing. And so, the skeleton composed of aggregates located on SFCs has better bearing and transferring loading capacity;
(3) Compared to SMA-16 and OGFC-16, AC-16 exhibits a higher number and total length of SFCs, a smaller average length of SFCs, and a lower average strength of SFCs. The SFCs of AC-16 exhibits better linearity. However, the average aggregate number located in a single SFC is smaller than that of SMA-16 and OGFC-16. Consequently, SMA-16 and OGFC-16 have better load carrying and transfer capacity than AC-16;
(4) For any type of MAM, approximately 90% of SFCs can only transmit external loads downward through 3–5 aggregates. The average direction angle of SFCs formed by fine aggregates is significantly higher than those formed by coarse aggregates. This indicates that the load transfer range of MAMs composed of fine aggregates is noticeably larger, leading to lower loading transfer efficiency.

Author Contributions: Conceptualization, Y.G. and G.L.; methodology, G.L.; software, Y.G.; validation, Y.G., G.L. and N.J.; formal analysis, Y.G.; investigation, Y.G.; resources, G.L.; data curation, Y.G.; writing—original draft preparation, Y.G.; writing—review and editing, G.L.; visualization, Y.G.; supervision, N.J.; project administration, G.L.; funding acquisition, G.L. All authors have read and agreed to the published version of the manuscript.

Funding: This research was supported by the National Natural Science Foundation of China (52208448), the Double Innovation Doctor of Jiangsu (JSSCBS20221503), the Graduate Innovation Program of China University of Mining and Technology (2024WLJCRCZL057), and the Postgraduate Research and Practice Innovation Program of Jiangsu Province (KYCX24_2808). The authors gratefully acknowledge their financial support.

Data Availability Statement: The data used to support the findings of this study are included within the article.

Conflicts of Interest: The authors declare no conflicts of interest.

References

1. Sun, Z.Q.; Han, J.N.; Liu, P.D.; Xu, S.L.; Yi, J.; Li, Y. Study on dimensionality reduction method for the micro calculation of asphalt mixtures based on stereology. *J. Munic. Technol.* **2023**, *41*, 8–17.
2. Fang, M.; Park, D.; Singuranayo, J.L.; Chen, H.; Li, Y. Aggregate gradation theory, design and its impact on asphalt pavement performance: A review. *Int. J. Pavement Eng.* **2018**, *20*, 1408–1424. [CrossRef]
3. Cai, X.; Wu, K.H.; Huang, W.K.; Wan, C. Study on the correlation between aggregate skeleton characteristics and rutting performance of asphalt mixture. *Constr. Build. Mater.* **2018**, *179*, 294–301. [CrossRef]
4. Guo, H.; Zhao, Y.; Zhang, D.; Shang, M. Study of movement of coarse aggregates in the formation process of asphalt mixture in the laboratory. *Constr. Build. Mater.* **2016**, *111*, 743–750. [CrossRef]
5. Wang, X.; Gu, X.; Jiang, J.; Deng, H. Experimental analysis of skeleton strength of porous asphalt mixtures. *Constr. Build. Mater.* **2018**, *171*, 13–21. [CrossRef]
6. Sun, S.; Li, P.; Akhtar, J.; Su, J.; Dong, C. Analysis of deformation behavior and microscopic characteristics of asphalt mixture based on interface contact-slip test. *Constr. Build. Mater.* **2020**, *257*, 119601. [CrossRef]
7. Sun, C.; Li, P.; Niu, B.; Xu, Y.; Zhang, W. Structure stability and shear failure behaviors of asphalt mixtures from the perspective of aggregate particle migration. *Constr. Build. Mater.* **2023**, *408*, 133653. [CrossRef]
8. Ma, T.; Zhang, D.; Zhang, Y.; Hong, J. Micromechanical response of aggregate skeleton within asphalt mixture based on virtual simulation of wheel tracking test. *Constr. Build. Mater.* **2016**, *111*, 153–163. [CrossRef]
9. Ding, X.; Ma, T.; Gao, W. Morphological characterization and mechanical analysis for coarse aggregate skeleton of asphalt mixture based on discrete-element modeling. *Constr. Build. Mater.* **2017**, *154*, 1048–1061. [CrossRef]
10. Ding, X.; Ma, T.; Huang, X. Discrete-Element Contour-Filling Modeling Method for Micromechanical and Macromechanical Analysis of Aggregate Skeleton of Asphalt Mixture. *J. Transp. Eng. B-Pave.* **2019**, *145*, 04018056. [CrossRef]

11. Wang, S.; Miao, Y.; Wang, L. Investigation of the force evolution in aggregate blend compaction process and the effect of elongated and flat particles using DEM. *Constr. Build. Mater.* **2020**, *258*, 119674. [CrossRef]
12. Cai, X.; Tang, H.Z.; Yang, X.C.; Nie, G.H.; Liu, X.Y.; Wu, K.H.; Huang, W.K. Identification of stress transfer in asphalt mixtures based on a reconstruction analysis of the simplified coarse aggregate skeleton. *Constr. Build. Mater.* **2023**, *370*, 130605. [CrossRef]
13. Chang, M.; Huang, P.; Pei, J.; Zhang, J.; Zheng, B. Quantitative Analysis on Force Chain of Asphalt Mixture under Haversine Loading. *Adv. Mater. Sci. Eng.* **2017**, *2017*, 7128602. [CrossRef]
14. Chang, M.; Pei, J.; Zhang, J.; Xing, X.; Xu, S.; Xiong, R.; Sun, J. Quantitative distribution characteristics of force chains for asphalt mixtures with three skeleton structures using discrete element method. *Granul. Matter* **2020**, *22*, 87. [CrossRef]
15. Shi, L.W.; Wang, D.Y.; Xiao, X.; Qin, X. Meso-structural characteristics of asphalt mixture main skeleton based on meso-scale analysis. *Constr. Build. Mater.* **2020**, *232*, 117263. [CrossRef]
16. Shi, L.W.; Xiao, X.; Wang, X.; Liang, H.H.; Wang, D.Y. Mesostructural characteristics and evaluation of asphalt mixture contact chain complex networks. *Constr. Build. Mater.* **2022**, *340*, 127753. [CrossRef]
17. Jin, C.; Wan, X.; Yang, X.; Liu, P.; Oeser, M. Three-Dimensional Characterization and Evaluation of Aggregate Skeleton of Asphalt Mixture Based on Force-Chain Analysis. *J. Eng. Mech.* **2021**, *147*, 04020147. [CrossRef]
18. Jin, C.; Wang, S.; Liu, P.; Yang, X.; Oeser, M. Virtual modeling of asphalt mixture beam using density and distributional controls of aggregate contact. *Comput. Aided Civ. Infrastruct. Eng.* **2023**, *38*, 2242–2256. [CrossRef]
19. Liu, G.; Pan, Y.; Zhao, Y.; Zhou, J.; Li, J.; Han, D. Research on Asphalt Mixture Force Chains Identification Criteria Based on Computational Granular Mechanics. *Can. J. Civ. Eng.* **2020**, *48*, 763–775. [CrossRef]
20. Liu, G.; Han, D.; Zhao, Y.; Zhang, J. Effects of Asphalt Mixture Structure Types on Force Chains Characteristics Based on Computational Granular Mechanics. *Int. J. Pavement Eng.* **2020**, *223*, 1008–1024. [CrossRef]
21. Liu, G.; Han, D.; Zhu, C.; Wang, F.; Zhao, Y. Asphalt-Mixture Force Chains Length Distribution and Skeleton Composition Investigation Based on Computational Granular Mechanics. *J. Mater. Civ. Eng.* **2021**, *33*, 04021033. [CrossRef]
22. *JTG F40-2004*; Technical Specification for Construction of Highway Asphalt Pavement. Ministry-of-Transport-of-the-People's-Republic-of-China: Beijing, China, 2004.
23. Liu, G.; Han, D.; Jia, Y.; Zhao, Y. Asphalt mixture skeleton main force chains composition criteria and characteristics evaluation based on discrete element methods. *Constr. Build. Mater.* **2022**, *323*, 126313. [CrossRef]
24. Liu, G.; Zhu, C.; Han, D.; Zhao, Y. Asphalt mixture force chains morphological characteristics and bearing capacities investigation using discrete element method. *Int. J. Pavement Eng.* **2023**, *24*, 2168660. [CrossRef]
25. Wang, H.; Zhou, Z.H.; Huang, W.L.; Dong, X.Y. Investigation of asphalt mixture permanent deformation based on three-dimensional discrete element method. *Constr. Build. Mater.* **2021**, *272*, 9. [CrossRef]
26. Hu, J.Y.; Ma, T.; Ma, K.; Xu, J. Three-dimensional discrete element simulation on degradation of air voids in double-layer porous asphalt pavement under traffic loading. *Constr. Build. Mater.* **2021**, *313*, 13. [CrossRef]
27. Zhu, J.Q.; Ma, T.; Lin, Z.H.; Zhu, H.R. Effect of aggregate structure on load-carrying capacity and deformation resistance of porous asphalt concrete based on discrete-element modelling. *Int. J. Pavement Eng.* **2022**, *23*, 4023–4033. [CrossRef]
28. *JTG E40-2007*; Test Methods of Soils for Highway Engineering. Ministry-of-Transport-of-the-People's-Republic-of-China: Beijing, China, 2007.
29. *JTG E20-2011*; Standard Test Methods of Bitumen and Bituminous Mixtures for Highway Engineering. Ministry-of-Transport-of-the-People's-Republic-of-China: Beijing, China, 2011.
30. Chen, J.; Li, H.; Wang, L.; Wu, J.; Huang, X. Micromechanical characteristics of aggregate particles in asphalt mixtures. *Constr. Build. Mater.* **2015**, *91*, 80–85. [CrossRef]
31. Zhang, W.; Zhou, J.; Zhang, X.; Zhang, Y.; Liu, K. Quantitative investigation on force chain lengths during high velocity compaction of ferrous powder. *Mod. Phys. Lett. B* **2019**, *33*, 1950113. [CrossRef]
32. Wang, J.-a.; Yang, L.; Li, F.; Wang, C. Force chains in top coal caving mining. *Int. J. Rock Mech. Min. Sci.* **2020**, *127*, 104218. [CrossRef]